

# Title: Brittle Creep and Brittle Failure of Rocks: a reformulation of the wing crack model

Authors: Yves Bernabé<sup>1</sup> & Matej Pec<sup>1\*</sup>

<sup>1</sup> Department of Earth Atmospheric and Planetary Sciences, Massachusetts Institute of Technology, 77 Massachusetts Ave., Cambridge, MA-02139

\*E-mail: mpec@mit.edu

## Abstract:

We propose a reformulation of the wing crack model of brittle creep and brittle failure. Experimental studies suggest that the mechanical interactions of sliding and tensile wing cracks are complex, involving formation, growth and coalescence of multiple tensile, shear and mixed-mode cracks. Inspired by studies of failure in granular media, we propose that these complex mechanical interactions lead to the formation of micro shear-bands, which, in turn, develop longer wing cracks and interact with a wider volume of rock to produce larger shear bands. This process is assumed to indefinitely continue at greater scales. We assume the original wing crack formalism is applicable to micro shear-band formation, with the difference that the half-length,  $a$ , of the characteristic micro shear band is allowed to increase with deformation (i.e. wing crack growth). In this approach, the dimensionless shear band half-length  $A$  is related to the dimensionless wing crack length  $L$  by a function,  $A(L) = 1 + f(L)$ , where  $f(L)$  embodies the entire process of shear band formation, growth and interaction with other shear bands and flaws and the problem is then to identify its proper form. We compare the model predictions for various classes of functions  $f(L)$  to experimental brittle creep data. Although a very large class of functions reproduce the classic sequence of tri-modal creep, we found that only the simple power law  $f(L) = (L/\Lambda)^q$  generated creep curves consistent with published creep data of rocks. Similar accord was also obtained with experimental brittle failure data.

## Plain language summary:

Rocks close to Earth's surface deform by breaking. Breaking can occur abruptly if the load the rocks bear increases rapidly. Breaking can however also occur over much longer times without changes to the load during a process called brittle creep. Observations suggest that breaking occurs due to growth and linkage of many small-scale flaws present in the rock. The details of this growth and linkage process, however, are very complex which complicates our ability to assess when rocks will ultimately break. Here we develop a model that simplifies the details of these small-scale interactions between large populations of flaws into a simple functional form. We analyze a number of possible functional forms and find that the simplest power law form yields good agreement with experimental data. Our model reproduces the behavior observed in brittle creep experiments where, after a step increase in load, the initially rapid rate of deformation first slows down, reaches a transitory steady-state and then accelerates until final failure occurs. Our model hence improves our ability to predict when failure will occur and presents a step towards mitigating the hazards associated with rock failure.

## Highlights:

- Sliding cracks and their wing cracks interact with nearby flaws to form shear bands, which coalesce to form shear bands at greater scales.
- Formation, growth and coalescence of shear bands is self-similar over a range of length-scales and is expressed by a power law function.

- The model naturally reproduces trimodal creep curves and returns experimentally determinable quantities.

## 1. Introduction

Deformation in Earth's upper crust is dominated by fracturing and frictional sliding resulting in macroscopically "brittle" behavior. Fractures occur over a range of length scales from intragranular microscopic cracks to fault zones spanning plate boundaries that host destructive earthquakes. The stress in the upper crust is limited by frictional sliding on favorably oriented faults (e.g. Zoback and Zoback 2007) and therefore much focus was dedicated to the problem of sliding frictional interfaces which are the end-product of brittle failure (e.g. Marone 1998, Dietrich 2007). Brittle creep and brittle failure that precede the formation of a through-going fault are relatively less studied phenomena, but nevertheless critical to our understanding of the long-term behavior of the crust and the earthquake cycle (e.g. Brantut et al. 2013, Main 2000). These phenomena will be the focus of the present contribution.

### 1.1 Background: the wing crack model

In the laboratory, rocks are typically tested under either constant stress or constant strain rate boundary conditions (or more precisely under constant load or constant displacement rate boundary conditions). Typical stress-strain-time plots obtained for both types of tests are schematically illustrated in figure 1. Under constant stress, rocks exhibit trimodal creep curves. Namely, decelerating "primary creep" occurs after the initial change in stress, followed by a transitory, apparent steady state "secondary creep", which eventually gives way to accelerating "tertiary creep" and failure (figure 1, left diagram). In constant strain rate tests, rocks first deform elastically (albeit, often non-linearly) until the yield point (i.e., onset of inelastic deformation), followed by strain hardening and accumulation of permanent strain. The axial stress eventually reaches a maximum (peak stress or strength), at which point a fault starts developing and the rock weakens to a stress level dictated by the residual friction on the fault (figure 1, right diagram). This macroscopic behavior is controlled by the activation, propagation and interactions of cracks in the rocks in the brittle regime. Loading conditions in nature are generally more complex than those employed in experiments, nevertheless laboratory tests can provide valuable insights into the micromechanics of brittle creep and brittle failure

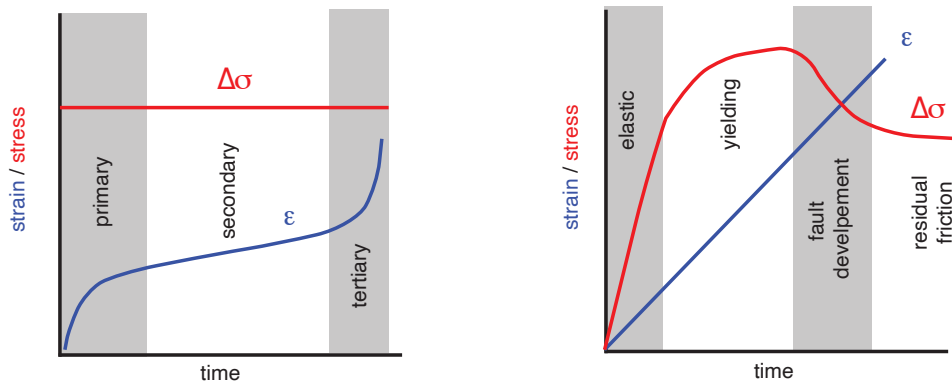


Figure 1. Schematic of typical curves of stress and strain versus time recorded in laboratory constant stress (left diagram) and constant strain rate tests (right diagram).

We are trying, here, to revisit the wing crack model of brittle failure and brittle creep. The wing crack model attributes the rock inelastic deformation leading to failure to tensile cracks that emanate from the tips of the largest pre-existing microcracks undergoing frictional shear. These activated microcracks are called the dominant cracks and are represented in the model by a single characteristic crack length,  $2a_0$ , and their inclinations with respect to the remotely applied principal stresses,  $\sigma_3 < \sigma_2 < \sigma_1$ . The resolved shear

stress is maximum in cracks oriented parallel to the intermediate stress  $\sigma_2$  and inclined with respect to the minimum stress  $\sigma_3$  by an angle  $\beta = 45^\circ$  (figure 2). The model assumes that the dominant cracks verify these optimal conditions, implying that the intermediate stress plays no role in the process of rock failure except for controlling the orientation of the final fracture. We will not attempt to modify this assumption in our model. A discussion of the effect of  $\sigma_2$  is considered out of the scope of the present paper.

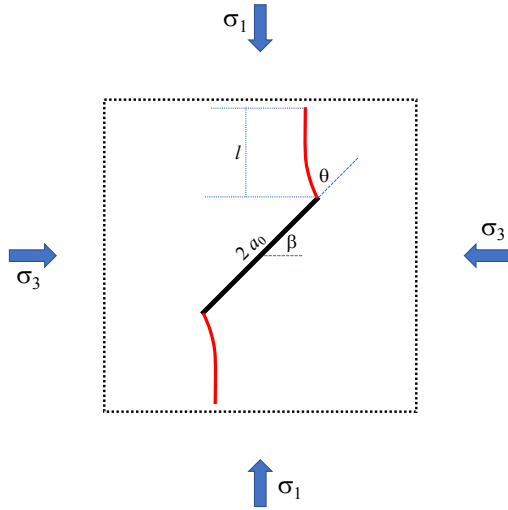


Figure 2. Schematic of a sliding microcrack and the associated wing cracks. The intermediate stress  $\sigma_2$  is normal to the figure plane. The angle  $\beta$  is, hereafter, assumed to be  $45^\circ$ .

In the idealized conditions depicted in figure 2, the wing cracks are curved. The angle  $\theta$  they form with the dominant microcrack changes during propagation, starting at about  $70^\circ$  at initiation and decreasing until the wing cracks become parallel to  $\sigma_1$ . Assuming  $\beta = 45^\circ$ , the normal stress and the resolved shear stress on the dominant microcrack are:

$$\sigma_N = \frac{1}{2} (\sigma_1 + \sigma_3) \quad (1)$$

$$|\tau| = \frac{1}{2} (\sigma_1 - \sigma_3) \quad (2)$$

Part of the shear stress is balanced by friction. The effectively active shear stress is therefore given by:

$$|\tau_{\text{eff}}| = |\tau| - \mu \sigma_N \quad (3)$$

where  $\mu$  is the friction coefficient and the condition  $|\tau| \geq \mu \sigma_N$  imposes  $\sigma_1/\sigma_3 \geq (1-\mu)/(1+\mu)$ . Note that we are using the geophysics convention that compressive stresses are positive.

The mode I stress intensity factor,  $\kappa_I$ , of a wing crack is a complex function of the remotely applied principal stresses, the length  $2a_0$  of the dominant crack, the wing crack length  $l$ , and, the angles  $\beta$  and  $\theta$  (figure 2). A number of models have been published (see Baud et al., 1996, for a review). Although they differ in some details depending on how the curvature of the wing cracks and other such features are treated, they all consist of the sum of two terms, one driving and one resisting wing crack propagation. Here, we consider the simple model from Kachanov (1982) (also used in Brantut et al., 2013):

$$\kappa_I = -1.15 |\tau_{\text{eff}}| \sqrt{\pi a_0} + \sigma_3 \sqrt{\pi l / 2} \quad (4)$$

Despite its simplicity (e.g., the wing crack curvature is ignored), the Kachanov model considers 3D penny shape microcracks and not 2D cracks like many other models. The model predicts that wing cracks will form when the initial stress intensity factor is larger than the rock fracture toughness,  $|\kappa_0| = 1.15 |\tau_{\text{eff}}| \sqrt{\pi a_0} \geq |\kappa_{Ic}|$ , or, in other words, when  $|\tau_{\text{eff}}|$  exceeds a critical shear stress  $\tau_c = |\kappa_{Ic}| / (1.15 \sqrt{\pi a_0})$ . The first (driving) term in equation 4 expresses the wedging effect of shear displacements at the tips of the dominant crack. The second (resistant) term depends on  $l$  and accounts for wing crack closure caused by  $\sigma_3$ . The two terms have different signs, causing  $|\kappa_I|$  to decrease with increasing  $l$ . Wing crack growth will therefore stop when  $\kappa_I$  becomes equal to  $\kappa_{Ic}$ , or, in other words, when the wing

crack length reaches  $l_0 = a_0 (1.15 (|\tau_{\text{eff}}| - \tau_c) / \sigma_3)^2$ . This ultimate crack arrest means that the behavior of a single wing crack system cannot be used to model brittle failure except, perhaps, in uniaxial compression conditions (increasing  $\sigma_1$  and  $\sigma_3 = \sigma_2 = 0$ ), when the wing cracks eventually intersect the sample edges (i.e., axial splitting). But this difficulty can be resolved by recognizing that the rock contains a broad population of mechanically interacting flaws. Interacting dominant cracks are expected to experience an increase of  $|\kappa_1|$  during wing crack extension. The currently published crack interaction models are all variations of the model developed by Ashby and Hallam (1986) and Ashby and Sammis (1990). In this model, the dominant microcracks are assumed to form linear arrays parallel to the maximum stress  $\sigma_1$ . Their growing wing cracks are therefore colinear and, owing to their mutual influence, the remotely applied lateral stress  $\sigma_3$  is locally reduced in the ligaments between neighboring wing cracks by a quantity  $\sigma_i$ . This causes a decrease of the resistant term,  $(\sigma_3 - \sigma_i) \sqrt{\pi l / 2}$ , and allows further propagation and finally coalescence of the wing cracks. The wing cracks thus form columns parallel to the maximum stress  $\sigma_1$ , which ultimately fail, owing to the classic buckling instability of slender columns. The intrinsic weakness of this model is the assumption of a very specific geometrical structure of the dominant microcracks, which is very unlikely to be found in a natural material. Nevertheless, the model has been quite successfully applied to experimental rock deformation and failure data (see the review by Brantut et al., 2013).

## 1.2 Background: crack coalescence

Since the early work of Horii and Nemat-Nasser (1985), the interaction and coalescence of wing cracks in conditions of uniaxial and biaxial compression have been experimentally investigated in a variety of materials, including rocks (see the comprehensive review of Wong, 2008). One important result is that biaxially loaded samples containing two parallel, cm-scale man-made crack-like flaws produced strongly different coalescence patterns depending on their relative positions and inclinations with respect to the applied principal stresses (e.g., Wong and Einstein, 2009ab; Lin et al., 2021). In Lin et al. (2021), a scalar measure of the strain field was determined as a function of time using digital image correlation analysis, allowing identification of the fissures developing and coalescing around the initial flaws. In the configuration shown in figure 3 (a schematic partial reproduction of Lin et al.'s figure 12), the wing cracks emanating from the inclined flaws merged and two new ones were created on the sides, forming a column aligned with  $\sigma_1$  quite similar to the structure assumed in the Ashby-Hallam-Sammis model. However, the unstable buckling of the column predicted in the Ashby-Hallam-Sammis model was not observed, perhaps because the experiment was prematurely stopped.

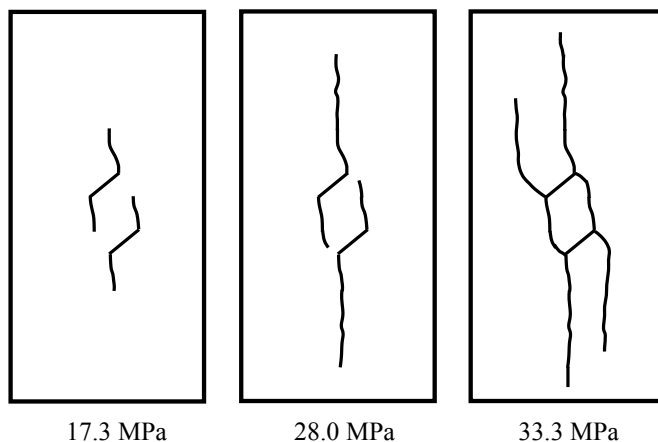
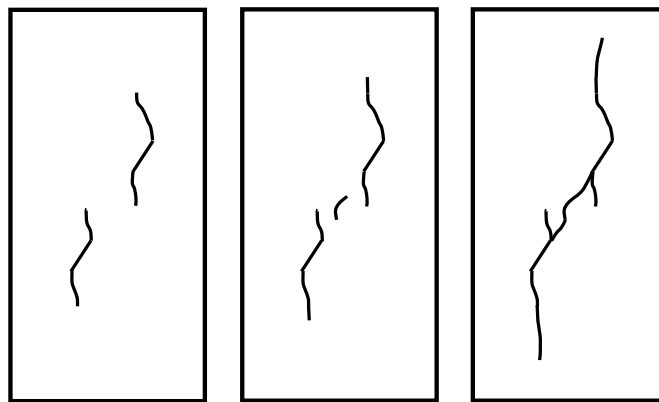


Figure 3. Simplified reproduction of figure 12 of Lin et al. (2021). The boxes show the outlines of growing wing cracks at the surface of a mortar slab containing two cm-scale flaws. The slab was subjected to uniaxial compression (the values of the axial stress is indicated below each box). The initial flaws are positioned such that the wing cracks merge and new tensile cracks are produced from the other side of the sliding flaws.

In other configurations of the initial flaws, very different coalescence patterns occurred, in which the inclined shear cracks themselves were actively involved. For example, a separate, small shear crack formed between two nearly aligned initial flaws and eventually merged with both of them, completely bridging the ligament (figure 4). Very complex bridging structures combining tensile, shear and mixed mode cracks were also observed in other configurations of the initial flaws.



19.8 MPa

25.3 MPa

32.2 MPa

Figure 4. Simplified reproduction of figure 7 of Lin et al. (2021). Here the position of the initial flaws leads to the formation of a shear crack and the eventual bridging of the ligament between the initial flaws.

Similar coalescence patterns were produced in samples of Carrara marble and molded gypsum (Wong and Einstein, 2009ab). For example, nearly aligned flaws produced bridging shear cracks, while merging of the tensile wing cracks occurred when the flaws were shifted to form a 90° angle. Combinations of shear, tensile and mixed mode bridging cracks were observed in other cases.

## 2. The model

### 2.1 The concept: micro to macroscopic shear bands

Despite the general similarity of the results described above, important differences were noted in materials with distinct internal structures. For example, development of a secondary crack was usually preceded in Carrara marble by an increase in light reflectivity (whitening) of the sample surface in a thin region exactly delineating the path of the future secondary crack (Wong, 2008; Wong and Einstein, 2009ab). These “white patches” visible on the sample surface prior to cracking can be attributed to the formation and accumulation of damage in highly strained thin zones. This explanation implies the existence, in the material, of a population of very small defects and microcracks (invisible to the eye or even a very high-resolution camera) that are activated by the amplified stresses around the large cm-scale flaws. White patches were not observed in molded gypsum, a microgranular material that was fabricated using procedures specifically designed to ensure excellent homogeneity. Lajtai (1974) similarly noticed the formation and growth of damaged shear zones at the tips of a sheared cm-scale synthetic crack in a biaxially stressed plaster slab. Evidence of interaction of large propagating cracks with smaller flaws is also reported in Brantut et al. (2014a). Their figure 12 shows examples of, on one hand, very smooth and rectilinear wing cracks in homogeneous sparitic calcite cement and, on the other, rough and tortuous cracks traversing microgranular micritic aggregations. As in rocks, failure of unconsolidated granular aggregates is generally observed to entail strain localization on shear bands. The initiation and growth of shear bands in granular materials has been extensively investigated experimentally and numerically (e.g., see Desrues, 1990, and references therein). One important observation is that the first stage of strain localization consists in the formation of multiple, separate micro shear bands. With increasing stress, some of these micro shear bands interact with neighboring ones, coalesce and eventually develop into macroscopic shear bands (Desrues and Andó, 2015). Similar scenarios have been observed in rocks. For example, figure 16 in Brantut et al. (2013) shows the hypocenter locations of acoustic emissions recorded during a creep test of a granite

sample. The distribution of hypocenters is random and featureless during primary and secondary creep but becomes strongly concentrated during tertiary creep in a region largely coincident with the final shear fracture (see also, Lockner et al., 1992; Lockner, 1993; Fortin et al., 2009; Fortin et al., 2010).

Here, we follow a similar concept. Natural flaws and microcracks in rocks have a very broad distribution of sizes. The (largest and most favorably oriented) dominant cracks are the first to develop wing cracks, which, as discussed above, are bound to interact with nearby minor flaws. We posit that this process will generally result in the development, near the tip of the dominant crack, of a complex array of microcracks (formed in tensile, shear and mixed mode) that globally deforms in shear. For lack of a better term, we will use the granular material terminology and call these structures micro shear bands. We emphasize that this term is meant to cover a broad range of damage structures, from simple merged shear cracks to inclined zones of crushed material. All these structures share a greater susceptibility to deform in shear than their surrounding, hence our choice to refer to them as shear bands. Shear cracks and micro shear bands similarly slide when submitted to sufficient shear stresses, although they may have different effective coefficients of friction. A wing crack should therefore develop at the outer edge of the shear band (figure 5). Note that wing cracks have indeed been observed to initiate from the edges of sheared microstructural objects other than microcracks. For example, Rawling et al. (2002) present SEM images of wing cracks emanating from the edges of sheared biotite grains in triaxially deformed samples of Four-mile gneiss (e.g., see their figure 9). Furthermore, owing to the overall increase in length, the wing crack emanating from a micro shear band will be longer than the initial one and, thus, have the capacity to interact with a greater volume of rock. It becomes therefore likely that two micro shear bands in favorable positions and orientations will coalesce to form even longer micro shear bands, from the edges of which increasingly long wing cracks will grow (figure 5). The model does not include an upper cut-off scale and the process is therefore assumed to continue at indefinitely increasing scales.

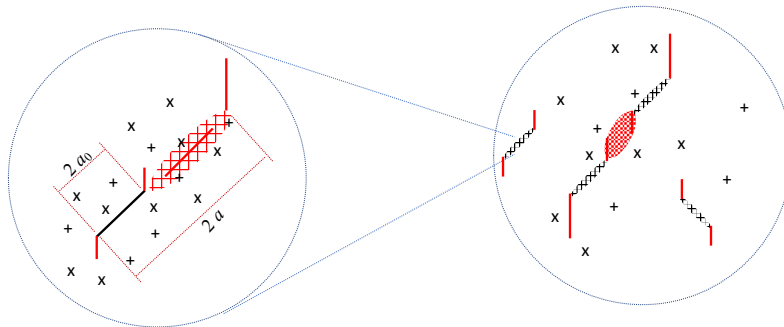


Figure 5. Schematic representation of mechanical interactions of cracks and flaws and the resulting micro shear band formation. The change of scale shown here is assumed to continuously take place at greater and greater scales.

## 2.2 Micro shear band model: brittle failure

We posit that the brittle deformation of rock illustrated in figure 5 can be described as the result of crack growth and coalescence around a representative dominant (or leading) micro shear band. Given the mechanical similarity of shear bands and sheared cracks, it is reasonable to assume that a leading micro shear band can be also modeled using the mathematical framework expressed in equation 4, the only difference being that the half-length  $a$  of the leading micro shear band increases during loading.

Since the second term of equation 4 describes the restraining effect of  $\sigma_3$  on wing crack expansion, it does not need to be modified. In the first term, the friction coefficient entering the definition of  $\tau_{\text{eff}}$  may depend on the internal structure of the shear band and thus vary during crack growth. For the sake of simplicity, we will assume that the friction coefficient of the micro shear bands remains approximately equal to that of the sheared cracks. Equation 4 then becomes:

$$\kappa_I = -1.15|\tau_{\text{eff}}|\sqrt{\pi a(l)} + \sigma_3\sqrt{\pi l/2} \quad (5)$$

where the half-length of the micro shear band is an increasing function of  $l$ . If we assume that wing crack growth is stable (as it has to be when the mechanical interactions are negligible) the crack arrest condition,  $\kappa_I = \kappa_{Ic}$ , yields:

$$-1.15(|\tau_{eff}| - \tau_c)\sqrt{\pi a(l)} + \sigma_3\sqrt{\pi l/2} = 0 \quad (6)$$

If  $|\tau_{eff}|$  is considered the independent variable (i.e., in constant loading rate tests), solving equation 6 for  $a(l)$  yields:

$$a(l) = l(\sigma_3/1.15(|\tau_{eff}| - \tau_c))^2 \quad (7)$$

which simply states that  $a(l)$  can be calculated if the dependence of  $l$  on  $|\tau_{eff}|$  is known. In this description, failure occurs with increasing  $|\tau_{eff}|$  when the leading shear band eventually reaches the sample boundaries. Rock failure tests, however, are usually carried out in constant strain rate conditions and not at constant loading rate as assumed by equation 7. In this case,  $l$  is the independent variable and prior knowledge of  $a(l)$  is needed to model brittle failure.

### 2.3 Micro shear band model: brittle creep

Following previous models of brittle creep, we introduce time dependence by assuming subcritical crack growth. In this case, wing crack propagation can proceed at constant stresses below the critical shear stress  $\tau_c$ . The initial stress intensity factor is  $|\kappa_0| = 1.15|\tau_{eff}|\sqrt{\pi a_0} < |\kappa_{Ic}|$  and equation 5 can be recast as:

$$\frac{\kappa_I}{\kappa_0} = \sqrt{a(l)/a_0} + \frac{\sigma_3}{\kappa_0}\sqrt{\pi l/2} \quad (8)$$

Equation 8 can be further simplified by using the following dimensionless variables and parameters:  $K_I = \kappa_I/\kappa_0$ ,  $A = a/a_0$  and  $L = l/l_0$ , where  $l_0 = 2a_0 (1.15 |\tau_{eff}|/\sigma_3)^2 = 2 \kappa_0^2/(\pi \sigma_3^2)$ , i.e., the maximum possible length of the wing cracks generated under the current state of stress at the tips of a microcrack of length  $2a_0$  in the absence of any mechanical interactions ( $l_0$  is thus an intrinsic property of the dominant microcracks of the undeformed rock). Note that  $l_0$  can be physically achieved when subcritical crack growth is operating since  $|\kappa_I|$  is allowed to drop to zero. We finally obtain:

$$K_I = \sqrt{A(L)} - \sqrt{L} \quad (9)$$

Although equation 9 is not a mechanistic model of crack coalescence, the function  $A(L)$  is effectively a closed-form expression of the results of the extremely complex and varied mechanical interactions underlying the formation and growth of micro shear bands. To do the job correctly,  $A(L)$  must satisfy a number of constraints. First, there are the trivial conditions that  $A(0) = 1$  and  $A(L)$  must be a monotonically increasing function. Thus,  $A(L)$  can be expressed as  $A(L) = 1 + f(L)$ , where  $f(L)$  is a monotonically increasing function verifying  $f(0) = 0$ . Most importantly,  $K_I$  must always be strictly larger than zero. Negative values obviously contradict the definition of  $K_I$  since  $\kappa_I$  and  $\kappa_0$  are both negative quantities. Moreover,  $K_I = 0$  implies crack arrest and is therefore incompatible with tertiary creep.

The simplest functions satisfying these conditions are the power law functions,  $f(L) = (L/\Lambda)^q$ , where  $\Lambda = \lambda/l_0$  is a dimensionless length scale representing the normalized distance that the wing crack must propagate to enter the vicinity of another microcrack or flaw, interact with it and therefore produce a substantial increase of  $K_I$ . Of course, other more complex functions such as the polynomials,  $f(L) = \sum_{i=1}^q C_i L^i$  (with  $C_i \geq 0$ ), can also meet the conditions above. We will focus here on the power laws  $f(L) = (L/\Lambda)^q$ , because they are the analytically simplest functions and, as will be discussed later, produced results in good agreement with experimental brittle creep data. We nevertheless investigated the polynomials  $f(L) = (1 + L/\Lambda)^q - 1$  (i.e.,  $A(L) = (1 + L/\Lambda)^q$ ) as thoroughly as  $f(L) = (L/\Lambda)^q$  but the results obtained were inconsistent with experimental brittle creep observations and will not be discussed in detail in the following text.

To illustrate how equation 9 works, it is convenient to consider the perfect square function  $A(L) = (1 + L/\Lambda)^2$  (see figure 6). Since the square root of  $A(L)$  is a linear function of  $L$ , the first term in equation 9 yields a family of straight lines with slopes increasing when  $\Lambda$  is decreased (the values of  $\Lambda$  are indicated in the same color as the corresponding lines in figure 6). The values of  $K_I$  are graphically measured as the vertical distance between these lines and the  $\sqrt{L}$  curve representing the second term of equation 9 (dashed

line in figure 6). Thus, in all cases,  $K_I$  first decreases (primary creep), reaches a minimum (secondary creep) and then increases indefinitely (tertiary creep). To satisfy the condition,  $K_I > 0$ , the colored straight lines in figure 6 are not allowed to intersect or tangentially touch the  $\sqrt{L}$  curve, thus limiting the values that  $\Lambda$  can take (in this example,  $\Lambda < \Lambda_c = 4$ ). We also note that increasing  $\Lambda$  causes a reduction of the minimum  $K_m$  of  $K_I$  and of the rate of increase of  $K_I$  in the second stage while the value  $L_m$  of  $L$  at the minimum increases (figure 6).  $K_m$  and  $L_m$  are key output parameters of the model since they identify the transition from primary to tertiary creep.

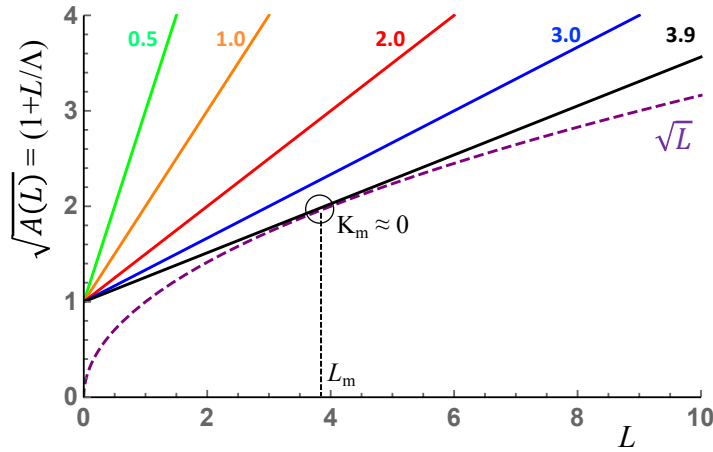


Figure 6. Graphic representation of equation 9 in the case of  $A(L) = (1 + L/\Lambda)^2$ . The vertical distance between the colored straight lines (the values of  $\Lambda$  for each line are indicated in matching colors) and the dashed purple curve is a measure of the stress intensity factor  $K_I$ . The position  $L_m$  of the minimum stress intensity factor  $K_m$  of the black curve is indicated by the small empty circle and the associated vertical dashed line. Note that  $K_m$  is nearly equal to zero in this case. See text for a detailed interpretation.

The consecutive  $K_I$ -decreasing and  $K_I$ -increasing stages illustrated in figure 6 were produced by the power laws  $f(L) = (L/\Lambda)^q$  with an exponent  $q \geq 2$  as well as all other functions  $f(L)$  examined in this study. These various  $f(L)$  functions, however, differed in the values of  $\Lambda_c$ ,  $K_m$  and  $L_m$  that they generated.

To assess the effect of the power law exponent  $q$  we examined the form of the curves of  $K_I$  versus  $L$  associated with  $f(L) = (L/\Lambda)^q$  for different values of  $q$  and  $\Lambda$  (the curves associated to  $q = 2$  to 6 and  $\Lambda = 1$  are shown in figure 7).

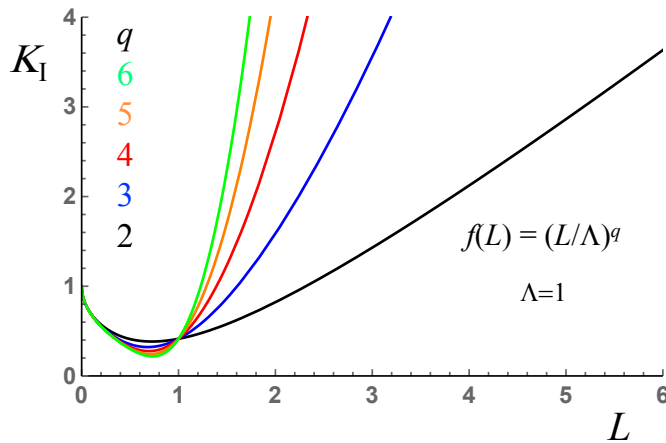


Figure 7. Examples of curves of stress intensity factor  $K_I$  versus wing crack length  $L$  associated with  $f(L) = (L/\Lambda)^q$  with  $\Lambda = 1$  for various values of the exponent  $q$  as indicated in matching colors. See text for a detailed discussion.



The limit  $\Lambda_c$  is analytically related to the exponent  $q$  through the expression,  $\Lambda_c = (q^{1/(1-q)} - q^{q/(1-q)})^{(1-q)/q}$  (see Appendix A for the derivation). According to this relation,  $\Lambda_c$  decreases from 2 to  $\sim 1.46$  when  $q$  is increased from 2 to 8. As mentioned earlier,  $\Lambda = \lambda/l_0$  represents the normalized distance, over which a wing crack must propagate to enter the vicinity of other microcracks and flaws and interact with them. It is important to note that this interaction distance depends both on the properties of the material being modeled and the state of stress considered. Indeed, the effect of the stress state is introduced through the normalization factor  $l_0 \propto (|\tau_{eff}|/\sigma_3)^2$  while the material is described by both  $l_0$ , which contains  $a_0$ , and  $\lambda$ , which can be understood as a characteristic flaw separation (or the inverse of the flaw density). Consequently, variations of  $\Lambda$  may represent either distinct materials with differing flaw densities or a single material subjected to various levels of stress. Thus, an increase of  $q$  indicates an increase of either the flaw density of the rock considered or the level of stress needed to allow brittle creep. We also note that the minimum stress intensity factor  $K_m$  along the  $K_I$  versus  $L$  curves decreased with increasing  $q$  while the corresponding  $L_m$  first decreased and then increased (figure 7).

Time dependence is then introduced in the model by assuming subcritical crack growth. According to this assumption, crack propagation proceeds gradually, starting at a stress intensity factor  $\kappa_0$  lower than  $\kappa_{IC}$ . Although different sub-critical crack growth models can be used, the most commonly reported in previous studies is based on the power law relation often called Charles' law (Charles, 1958; see also Wiederhorn and Boltz, 1970):

$$\frac{v}{v_0} = \left(\frac{\kappa_I}{\kappa_0}\right)^n \quad (10)$$

where  $v$  and  $v_0$  are propagation velocities of the wing cracks, and the exponent  $n$  usually takes very high values (between 10 and 50). Note that equation 10 is dimensionless and can be re-written  $V = K_I^n$ , with  $V = v/v_0$ , and then combined with equation 9 to yield:

$$V = \frac{dL}{dT} = (\sqrt{1 + f(L)} - \sqrt{L})^n \quad (11)$$

where the normalized time is defined as  $T = t/t_0 = t v_0/l_0$ . Using the previously discussed functions  $f(L) = (L/\Lambda)^q$ , equation 11 contains three parameters, the normalized flaw separation  $\Lambda$ , the power law exponent  $q$  and the subcritical crack growth exponent  $n$ . Since  $L$  is a strictly monotonic, increasing function of  $T$ , equation 11 can be numerically solved using the following simple procedure. First we construct a wing crack length series,  $L_i = (i - 1) dL$ , where  $dL$  denotes a small increment (e.g.,  $dL = 0.01$  or lower for more accuracy). We then use equation 10 to calculate the corresponding wing crack velocity series  $V_i$ . Finally, the time series  $T_i$  can be calculated using the recurrence  $T_{i+1} = T_i + dT_i$ , with  $dT_i$  calculated by numerical integration of  $dT_i = \int_{L_i}^{L_{i+1}} (\sqrt{1 + f(L)} - \sqrt{L})^{-n} dL$ . Examples of curves of  $V$  as a function of  $T$  corresponding to  $f(L) = (L/\Lambda)^q$  with  $\Lambda = 0.1, 0.5, 1., 1.4$  and  $1.75$ ,  $q = 2$  and  $4$ , and,  $n = 10$  are shown in figure 8.

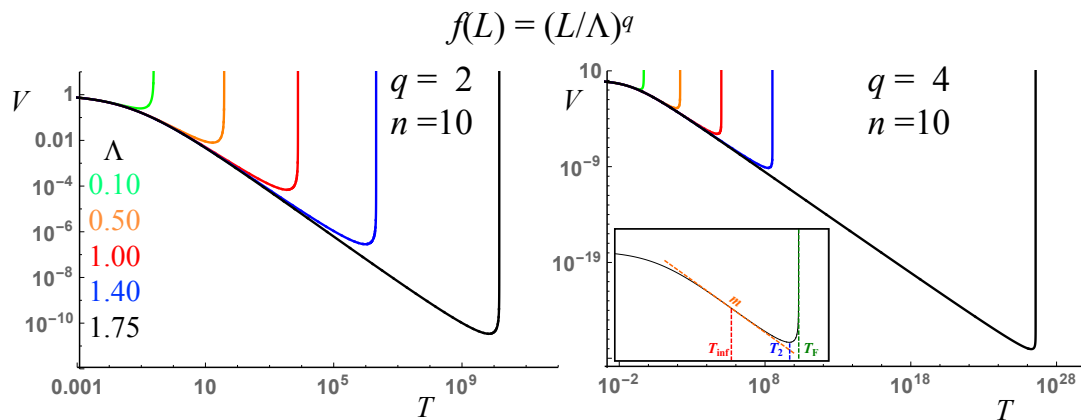


Figure 8. Examples of curves of wing crack growth rate  $V$  versus time  $T$  associated with  $f(L) = (L/\Lambda)^q$  for  $q = 2$  (left diagram) and  $4$  (right diagram). The values of  $\Lambda$  corresponding to each curve are indicated in matching colors (the subcritical crack growth exponent  $n$  was equal to 10 in all cases). The times  $T_{inf}$ ,  $T_2$  and  $T_F$ , and the exponent  $m$  are graphically defined in the inset. See text for a detailed discussion.

In all cases considered in this study, the  $V$  versus  $L$  curves displayed the same generic shape consistent with the three classic stages of creep. As illustrated in figure 8, the crack propagation velocity  $V$  first decreases gradually (decelerating or primary creep stage) down to a minimum value (secondary creep) and then sharply increases up to failure (accelerating or tertiary creep stage). The failure time  $T_F$  is obtained by integrating  $dT = dL/V$  for  $L$  increasing from 0 to infinity.

$$T_F = \int_0^\infty (\sqrt{1 + f(L)} - \sqrt{L})^{-n} dL \quad (12)$$

The integral of equation 12 is convergent for all values of  $\Lambda$  satisfying the condition  $\Lambda < \Lambda_c$  and all functions  $f(L)$  mentioned in previous sections. Figure 8 also shows that the decelerating stage consists of two segments, first the deceleration magnitude  $|dV/dT|$  increases and then, after an inflection point is passed, decreases down to zero (i.e., the point where the accelerating stage begins). Comparison of the right- and left-hand diagrams demonstrates that increasing the polynomial degree  $q$  (for a given  $\Lambda$ ) brings the minimum propagation velocity closer to zero, increases greatly the time to failure and strongly sharpens the transition to tertiary creep. Similar effects are produced by raising the subcritical crack growth exponent  $n$  (not shown in figure 8).

Based on the results described above, three key points can be identified along the curve of  $V$  versus  $T$ , namely, (1) the inflection point within the decelerating creep stage, (2) the minimum of the curve (note that this point is the limit between the primary and tertiary creep segments; it can therefore be interpreted as the center of a secondary creep segment), and (3) the failure point. These three points are distinguished by their respective time coordinates,  $T_{\text{inf}}$ ,  $T_2$  and  $T_F$  (see inset in figure 8). Furthermore, in a log-log plot, the tangent at the inflection point  $T_{\text{inf}}$  defines a local power law  $V \propto T^m$ , which becomes steeper with increasing  $\Lambda$  (see inset in figure 8). Although the individual normalized times  $T_2$  and  $T_F$  may be difficult to determine experimentally because the time normalization,  $T = t l_0/V_0$ , involves  $l_0$ , a quantity that may not be experimentally accessible, the ratio  $T_F/T_2$  is independent of normalization and can be measured in laboratory tests.

We measured  $T_F/T_2$  for  $f(L) = (L/\Lambda)^q$  in various conditions of  $\Lambda$ ,  $q$  and  $n$ . We observed that  $T_F/T_2$  strongly decreased with increasing  $\Lambda$  when  $q$  was equal to 2, changed to a much flatter, non-monotonic behavior with increasing  $q$  from 3 to 5, and eventually became a steadily but moderately increasing function of  $\Lambda$  for  $q = 6$  (figure 9, right diagram). In all cases,  $T_F/T_2$  approached a limit value of 2 for the largest  $\Lambda$ 's while a wide range, from as high 3 to as low as 1.6, was obtained for  $\Lambda$  near zero depending on the polynomial degree  $q$ .

Because inflection points are patently difficult to determine from noisy data,  $T_{\text{inf}}$  is not a practical parameter to use for comparison with experimental data, but the exponent  $m$  is independent of time normalization and can be estimated as a characteristic power law exponent of rock primary creep data. We calculated  $m$  for a variety of values of  $\Lambda$  and  $q$ . We observed that  $m$  showed approximately logarithmic dependence on  $\Lambda$  for different values of  $q$  (figure 9, left diagram). The calculated  $m$ 's increased from values between 0.2 and 0.5, depending on  $q$ , at low  $\Lambda$ 's to an upper limit of about 1 at  $\Lambda$ 's approaching  $\Lambda_c$  (figure 9, left diagram).

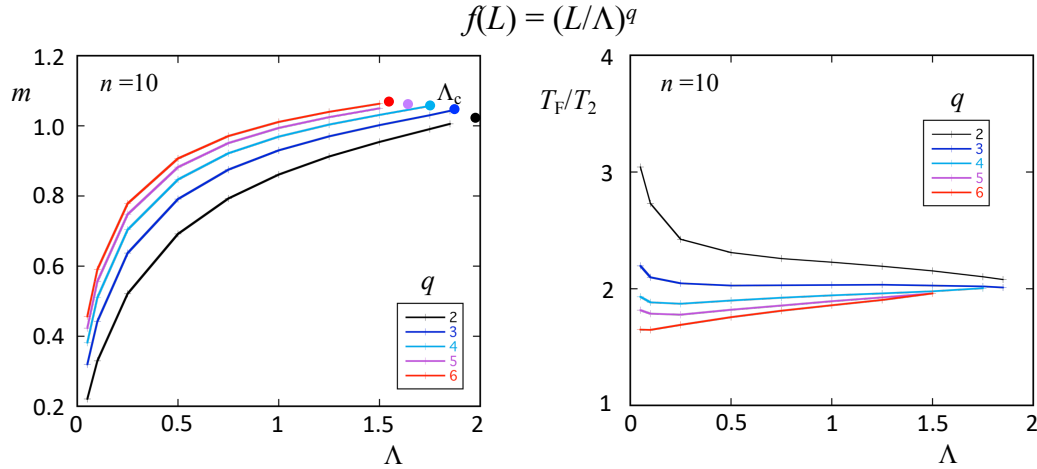


Figure 9. Examples of the predicted dependence of the primary creep exponent  $m$  (left diagram) and the failure time to secondary creep time ratio  $T_F/T_2$  (right diagram) on the characteristic flaw separation  $\Lambda$ . These curves correspond to the function  $f(L) = (L/\Lambda)^q$  with values of  $q$  indicated in matching colors (the subcritical crack growth exponent  $n$  was equal to 10 in all cases). The positions of the limit  $\Lambda_c$  for the different exponents  $q$  are indicated by colored solid dots in the left diagram. See text for a detailed discussion.

### 3. Discussion

#### 3.1 Comparison with experimental data: brittle creep

Testing this model against experimental data cannot be done directly since the essential wing crack parameters  $l$  and  $v$  cannot be measured in rock samples during deformation. Even, estimating the half-length  $a_0$  of the dominant flaws from SEM images of the undeformed rock is an extremely difficult and uncertain undertaking. We will assume here that the macroscopic creep strain rate  $\dot{\epsilon}'$  of a very large volume of material containing many dominant microcracks is linearly related to the wing crack propagation velocity  $v$ . Note that the (usually non-linear) relations between  $v$  and  $\dot{\epsilon}'$  derived in various versions of the Ashby-Hallam-Sammis model (e.g., Brantut et al., 2012) cannot be used in our model. Indeed, these relations only include the effect of wing cracks growth and neglect the shear displacements along the dominant microcracks. In our model, on the other hand, the macroscopic creep strain rate is mainly produced by formation and shearing of the micro shear bands. Accordingly, the experimental equivalent of the wing crack length  $l$  is the (inelastic) creep strain  $\epsilon$ . Note that there is no measurable equivalent of  $l_0$ , making it impossible to normalize experimental time so that it can be directly compared to the model dimensionless time  $T = t v_0 / l_0$ . However, the main output parameters of the model, the exponent  $m$  and the ratio  $t_F/t_2$  can be estimated from experimental creep curves spanning the three regimes from primary to tertiary creep without time normalization. Note that experimental data are necessarily afflicted by noise, mostly random fluctuations of the readings of the measuring devices but sometimes also errors caused by computer glitches. Published data sometimes contain “unphysical” features in the recorded signals, like sharp steps (i.e., points of extremely high strain rates) or oscillations (i.e., alternating positive and negative strain rates), which require specific removal treatments (the easiest being manually passing a smooth curve through the steps or oscillations). Since the combination of regularization techniques needed for differentiating the experimental  $\epsilon$  versus  $t$  data strongly depended on the particular data being analyzed, we did not attempt to develop a comprehensive data-treatment workflow. Each data set was individually processed, although we made every effort to maintain consistency.

We downloaded or digitized the published brittle creep data of Inada granite (Fujii et al., 1999), Thala limestone (Brantut et al., 2013), Etna basalt (hereafter labeled Etna basalt 1; Heap, 2009; Heap et al., 2011) and Darley Dale sandstone (Heap, 2009; Heap et al., 2009) and calculated the corresponding time-dependent strain rates. In the case of Darley Dale sandstone and Etna basalt 1 (Heap, 2009), preliminary constant strain rate tests at different effective confining pressures were performed to determine the rock strength defined as the peak effective differential stress  $\sigma_{\text{peak}} - \sigma_3$  (note that, in the following, all stresses will

be understood to be effective stresses, i.e., differences of the total stresses and pore pressures). Creep tests at the same effective confining pressure (30 MPa) and various effective differential stresses  $\sigma_1 - \sigma_3$  below the previously measured peak stresses were then carried out in samples from the same blocks (Heap, 2009). These tests are particularly interesting to us since the samples had presumably identical properties and microstructures but were subjected to different stresses. We therefore expected that the experimental data would yield values of  $T_F/T_2$  and  $m$  consistent with a single value of  $q$  and decreasing  $\Lambda$ 's with increasing creep stress. We also analyzed creep curves measured in basalt samples from a different outcrop on Mount Etna (hereafter labelled Etna basalt 2, Mansbach, 2022) and a cored well in Iceland (Xing et al., 2022), and, in thermally cracked glass cylinders (Mallet et al., 2014, 2015).

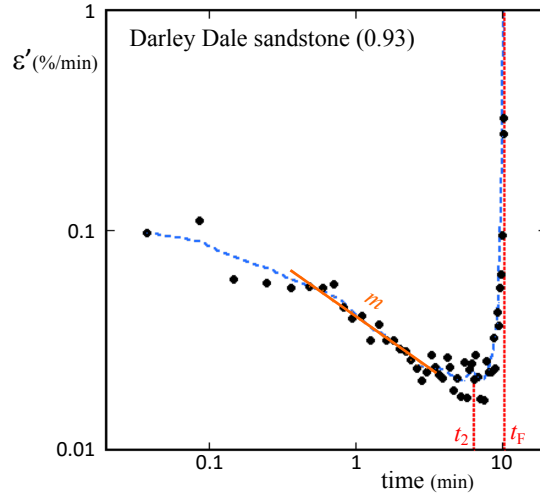


Figure 10. Example of a strain rate versus time curve calculated from a digitized experimental creep curve (here, a Darley Dale sandstone creep test at a creep to peak stress ratio of 0.93; Heap, 2009; Heap et al., 2009). Experimental data with (dotted blue line) and without smoothing (solid black dots) are shown. The estimates of  $t_F$ ,  $t_2$  and the primary creep exponent  $m$  are graphically indicated. See text for a detailed discussion.

The experimental curves of  $\log(\epsilon')$  versus  $\log(t)$  of these rock samples (e.g., figure 10) appear indeed similar to the theoretical curves of figure 8. We were, therefore, able to estimate the two primary output parameters,  $t_F/t_2$  and  $m$ , from these data. The time to failure  $t_F$  is easy to measure but  $t_2$  can be more challenging (note that superposing the smoothed creep curves and the original noisy ones is quite helpful to avoid unreasonable under- or overestimations of  $t_2$  and to estimate uncertainties). The inflection point within the decelerating stage is all but impossible to identify, but the power law exponent  $m$  can still be estimated by selecting a segment of data points at the center of the primary creep stage (see the example of figure 10; again superposing the smoothed and original data is a very useful precaution). Within the estimated uncertainties, the measured values of the ratio  $t_F/t_2$  ranged from about 1.5 to 2.2, and  $m$  from 0.4 to slightly over 1.

For comparison purposes, we superposed the experimental  $(m, t_F/t_2)$  data on the theoretical  $T_F/T_2$  versus  $m$  curves obtained by cross-plotting the numerical results for the function  $f(L) = (L/\Lambda)^q$  and constant values of  $q$ . Note that the theoretical curves converge from the left border to the vicinity of the point  $(m = 1; T_F/T_2 = 2)$ , thus delimiting a wedge-shaped region that excludes values of  $m$  significantly exceeding one. The experimental results are in good agreement with the model in the sense that the measured data points approximately fall within the allowed wedge-shaped region (figure 11). This observation also lends support to our assumption that the strain rate  $\epsilon'$  is linearly related to the wing crack propagation velocity  $v$ . Indeed, let's assume instead that  $\epsilon'$  is an arbitrary (monotonically increasing) function  $g$  of  $v$ . The experimental strain rate versus time curves (e.g., figure 10) should then be compared to curves of  $g(V)$  versus  $T$ , which should have similar shapes to the curves shown in Figure 8 but yield very different values of  $m$ . These changes would likely produce a very different Figure 11. They could significantly distort the region in  $(m;$

$T_F/T_2$ ) space allowed by the model and thus reduce or even destroy any agreement of model and experiments.

Although we cannot exclude that other functions besides  $(L/\Lambda)^q$  may yield similarly satisfactory results, we can definitely eliminate the function  $A(L) = (1 + L/\Lambda)^q$  (or  $f(L) = (1 + L/\Lambda)^q - 1$ ), which only generated values of  $T_F/T_2$  greater than 2 that are not consistent with more than half the experimental data. We surmise that the unfitness of the function  $A(L) = (1 + L/\Lambda)^q$  is shared by all polynomial functions combining terms of widely variable degrees in  $L/\Lambda$ , including linear and quadratic terms, which produce values of  $T_F/T_2$  significantly greater than 2. If this is true, we can, hereafter, safely limit our discussion to the simple power laws  $f(L) = (L/\Lambda)^q$ .

If the functions  $f(L) = (L/\Lambda)^q$  are indeed the appropriate functions for interpreting rock data, we can infer the values of  $q$  and  $\Lambda$  corresponding to each creep experiment. For example,  $q \approx 4$  fits both Inada granite and Thala limestone although a larger  $\Lambda$  is associated to the granite than the limestone ( $\Lambda \approx 0.5$  and  $0.1$ , respectively). It is tempting to interpret this result as indicating that the granite, whose low porosity (0.45%) presumably consists of long, thin microcracks, has a lower flaw density than a strongly heterogeneous, porous (17.5 %) carbonate. But it would be wrong to do so because  $\Lambda$  is normalized by  $l_0$ , an unknown quantity that could take very different values in these two rocks. The only other observation in support of taking large  $\Lambda$ 's as an indication of low flaw density is the fact that even larger values of  $\Lambda$  ( $> 1.5$ ) correspond to the two thermally cracked glass samples. Their microstructure, indeed, exclusively consists of cm-scale rather thin and smooth microcracks with intersections distant from each other by a few to tens of millimeters (Mallet et al., 2014).

Even though the absolute values of  $\Lambda$  are practically impossible to interpret, relative variations can be amenable to quantitative analysis. As mentioned earlier, creep experiments at different stress levels were carried in four samples of Etna basalt 1 extracted from the same block and a similar procedure was applied to three samples of Darley Dale sandstone (Heap, 2009). We therefore expect  $q$  to be constant in each rock, which is indeed observed for three of the Etna basalt 1 samples ( $q = 2$ ) and all the Darley Dale sandstone ones ( $q \approx 7$  or  $8$ ). We also note that the inverse of  $\Lambda$  can be expressed as a second-degree polynomial in  $\sigma_1$ :

$$\frac{1}{\Lambda} = C_0 - 2C_1\sigma_1 + C_2\sigma_1^2 \quad (13)$$

Indeed, combining equations 1 to 3 yields the linear expression,  $|\tau_{\text{eff}}| = a\sigma_1 - b$ , where the positive constants are given by  $a = (1-\mu)/2$  and  $b = \sigma_3(1+\mu)/2$ . By definition  $l_0$  is proportional to  $|\tau_{\text{eff}}|^2 = a^2\sigma_1^2 - 2ab\sigma_1 + b^2$  and so is  $1/\Lambda = l_0/\lambda$ , hence demonstrating equation 13. The positive constants  $C_0$ ,  $C_1$  and  $C_2$  are proportional to  $b^2/\lambda$ ,  $ab/\lambda$  and  $a^2/\lambda$ , respectively, and therefore obey the equality  $C_2/C_1 = C_1/C_0 = a/b$ .

We graphically estimated  $\Lambda \approx 0.40$ ,  $1.15$  and  $1.89$  for the three Etna Basalt 1 samples with  $\sigma_1/\sigma_{\text{peak}} = 0.97$ ,  $0.86$  and  $0.80$ , respectively. Using the values above, the curve of  $1/\Lambda$  versus  $\sigma_1/\sigma_{\text{peak}}$  is indeed very well fitted with a second-degree polynomial of the same form as in equation 13. The estimated constants  $C_0 = 32.9$ ,  $C_1 = 41.8$  and  $C_2 = 53.8$  yield ratios  $C_1/C_0 = 1.27$  and  $C_2/C_1 = 1.29$  within 1.5% of the theoretical equality. We applied the same analysis to the Darley Dale sandstone data. A value of  $q$  greater than 6 was needed, which posed some numerical problems because we had to use a much smaller increment  $dL$  of  $3 \times 10^{-5}$  to maintain an acceptable accuracy. Using  $q = 8$ , we obtained  $\Lambda \approx 0.27$ ,  $0.19$  and  $0.059$  for the creep stress levels  $\sigma_1/\sigma_{\text{peak}} = 0.84$ ,  $0.88$  and  $0.93$ , respectively, which yielded  $C_0 = 1560$ ,  $C_1 = 1930$  and  $C_2 = 2270$ , corresponding to ratios  $C_1/C_0 = 1.170$  and  $C_2/C_1 = 1.174$  in excellent agreement with the theoretical equality. Thus, the values of  $\Lambda$  fitting the Etna basalt 1 and Darley Dale sandstone experiments are quantitatively consistent with the creep stresses used in them.

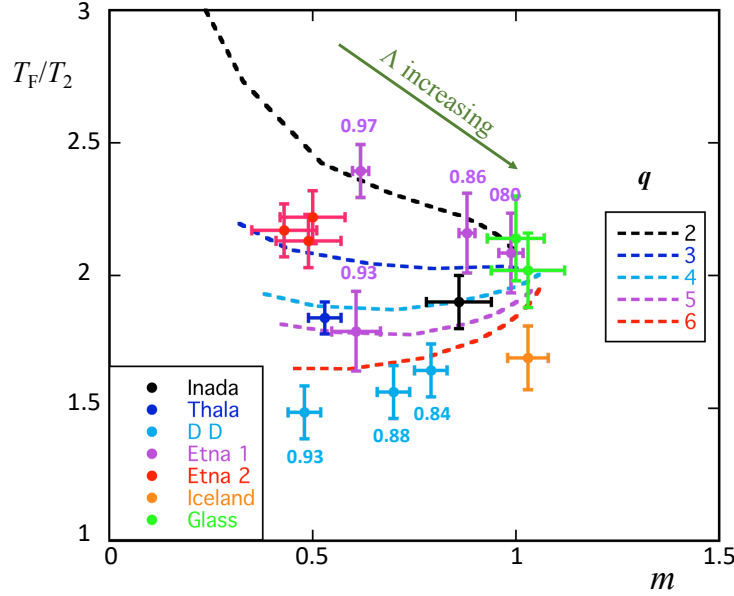


Figure 11. Experimental estimates of  $t_F/t_2$  and  $m$  for Inada granite (black), Thala limestone (dark blue), Darley Dale sandstone (light blue), Etna basalt 1 (purple), Etna basalt 2 (red), Iceland basalt (orange) and thermally cracked glass (green). The error bars indicate the estimated uncertainties of the calculated values of  $t_F/t_2$  and  $m$ . In the case of Darley Dale sandstone and Etna basalt 1, the creep stress levels ( $\sigma_1/\sigma_{\text{peak}}$ ) are shown above the data points in matching color. The theoretical curves of  $T_F/T_2$  versus  $m$  for the function  $f(L) = (L/\Lambda)^q$  and various values of the exponent  $q$  as indicated in the inset on the right side of the diagram, are superposed on the experimental data. The olive green arrow indicates the direction in which the theoretical interaction distance  $\Lambda$  increases in this diagram.

### 3.2 Comparison with experimental data: brittle failure in constant strain rate experiments

Since  $f(L) = (L/\Lambda)^q$  appears to yield an appropriate description of experimental creep data in a large variety of rocks, it is worth incorporating it in the failure model. Equation 6 thus becomes:

$$-1.15(|\tau_{\text{eff}}| - \tau_c) \sqrt{\pi a_0 \left(1 + \left(\frac{l}{\lambda}\right)^q\right)} + \sigma_3 \sqrt{\pi l/2} = 0 \quad (14)$$

Equation 14 can be written in dimensionless form using  $\tau^* = (|\tau_{\text{eff}}| - \tau_c)/\sigma_3$ ,  $l^* = l/(1.15^2 2a_0)$  and  $\lambda^* = \lambda/(1.15^2 2a_0)$  (note that the previously used normalization of  $l$  and  $\lambda$  to  $l_0$  is not possible here because the remotely applied stresses are not constant in constant strain rate experiments). Solving it for  $\tau^*$ , yields:

$$\tau^* = \sqrt{\frac{l^*}{1 + \left(\frac{l^*}{\lambda^*}\right)^q}} \quad (15)$$

Equation 15 can be used to model constant strain rate tests by calculating the variations of  $\tau^*$  associated to a constant rate of increase of  $l^*$ . We thus determined the  $\tau^*$  versus  $l^*$  curves for  $q$  varying from 2 to 12 and  $\lambda^*$  from 0.1 to 16. All curves go through a maximum,  $\tau^* = \tau^*_{\text{peak}}$ , analogous to rock peak strength at  $l^* = l^*_{\text{peak}}$  (see examples in figure 12). The right-hand side of equation 15 is sufficiently simple to allow determining the coordinates of the peak analytically, yielding:

$$l^*_{\text{peak}} = \lambda^*/(q-1)^{1/q} \quad (16)$$

$$\text{and} \quad \tau^*_{\text{peak}} = \sqrt{\frac{\lambda^*}{q} (q-1)^{\frac{q-1}{q}}} \quad (17),$$

which implies  $\tau^*_{\text{peak}} = \sqrt{l^*_{\text{peak}} (q-1)/q}$  (see derivation in appendix B). Thus,  $l^*_{\text{peak}}$  is proportional to  $\lambda^*$  (the pre-factor decreasing from 1 to  $\sim 0.757$  and then slightly increasing to  $\sim 0.784$ , when  $q$  is increased from 2 to  $\sim 4.6$  and finally 8). In the same range of  $q$ ,  $\tau^*_{\text{peak}}$  varies as the square root of  $\lambda^*$  (the pre-factor gradually increasing from  $\sim 0.707$  to  $\sim 0.828$ ). Although the definitions of  $\lambda^*$  and  $\Lambda$  are not identical, these two parameters are both related to the separation distance between microcracks and/or flaws, or, in other

words, inversely related to the flaw density. As intuitively expected, the model predicts that strength increases with decreasing flaw density (left diagram, figure 12).

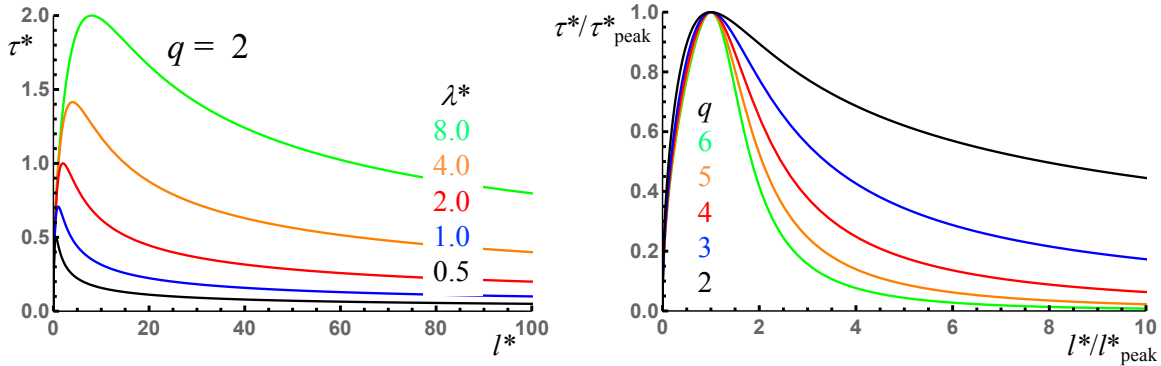


Figure 12. Examples of curves of normalized resolved shear stress  $\tau^*$  versus normalized wing crack length  $l^*$  for the function  $(l^*/\lambda^*)^q$  with  $q = 2$  and various values of the dimensionless flaw separation  $\lambda^*$  as indicated in matching colors (left diagram). Curves of  $\tau^*$  versus  $l^*$  normalized to their peak values  $\tau^*_{\text{peak}}$  and  $l^*_{\text{peak}}$ , respectively, for various values of  $q$  as indicated in matching colors (right diagram). Importantly, these curves are independent of the values of  $\lambda^*$  used to calculate them (in other words, variations of  $\lambda^*$  at constant  $q$  yield exactly coincident curves).

Interestingly, normalizing the shear stress and wing crack length to their values at the peak (i.e.,  $\tau^*/\tau^*_{\text{peak}}$  and  $l^*/l^*_{\text{peak}}$ ) produced exactly coincident curves for a given value of  $q$ , independent of  $\lambda^*$  (right diagram, figure 12). Thus,  $\lambda^*$  (equivalently, the flaw density) affects the values of  $\tau^*_{\text{peak}}$  and  $l^*_{\text{peak}}$  but not the shape of the curves. Instead, it is the power law exponent  $q$  which appears to control the shape of the  $\tau^*$  versus  $l^*$  curves, particularly the post-peak softening stage. Increasing values of  $q$  produce an increasingly sharp softening post-peak behavior (right diagram, figure 12). Note that, in the softening stage,  $\tau^*$  asymptotically approaches zero while  $l^*$  increases to infinity (figure 12). This implies that formation of new larger shear bands continues indefinitely at shear stresses ( $\tau_{\text{eff}}$ ) closer and closer to  $\tau_c$ , the shear stress, below which wing crack growth was not initially allowed. This property is due to the fact that the model does not include an upper scale limit and, therefore, does not allow formation of a through-going shear band like those ultimately occurring in (finite size) rock samples deformed to brittle failure.

Stress-strain curves measured in brittle materials are similar to the theoretical curves shown in figure 12. However, unlike the  $\tau^*$  versus  $l^*$  curves, which represent the results of exclusively inelastic processes, experimental stress-strain curves include both elastic and inelastic strains. For the purpose of comparison with the model, the axial strain,  $\varepsilon = \varepsilon_e + \varepsilon_i$ , measured in a constant strain rate test must be corrected of its elastic component  $\varepsilon_e$  so that only the inelastic strain  $\varepsilon_i$  remains. Elastic strains must obviously be dominant during the early stage of a constant strain rate test when the applied stress is too low to produce significant inelastic deformation. This elastic stage is usually identified as the upwardly curved segment, commonly observed at the beginning of the stress-strain curve (e.g., Heap and Faulkner, 2008). Along this segment, the axial Young's modulus  $E$  (i.e., the slope of the stress-strain curve) increases gradually owing to the closure of cracks normal to  $\sigma_1$  and reaches a maximum (i.e., inflexion point of the stress-strain curve) at  $\sigma_1 = \sigma_c$  that is generally assumed to mark the onset of inelastic deformation. The interpretation of the upwardly curved segment as purely elastic has generally been considered satisfactory in many studies where dilatancy was measured and/or acoustic emissions recorded (among others, Lockner et al., 1992; Lockner, 1993; Stanchits et al., 2006; Fortin et al., 2009; Fortin et al., 2010). However, even if the purely elastic stage of a given laboratory test is accurately identified, determining  $\varepsilon_e$  along the rest of the stress-strain curve cannot be done without extrapolation unless the elastic properties were actually measured at regular intervals, for example, by running small cyclic stress excursions (e.g., Bernabé et al., 1994). The use of such techniques, however, is extremely rare in practice. Here, we manually digitized the



stress-strain curves measured in Etna basalt 1 and Darley Dale sandstone by Heap (2009), since we had previously determined suitable values of  $q$  for these rocks, and attempted to construct models of the rocks Young's modulus as a function of stress and total axial strain. Our first attempt yielded values of  $(\sigma_{\text{peak}} - \sigma_c)/\sigma_3$  (i.e., the equivalent of  $\tau_{\text{peak}}^*$ ) that did not scale as the square root of  $\epsilon_{\text{peak}}$ , the inelastic strain at the peak of the stress-strain curve, as predicted by the model. However, fine-tuning the elastic model brought the results closer to the model prediction. Since the validity of the elasticity models cannot be checked independently, these efforts do not produce truly meaningful results and this approach was not pursued further.

#### 4. Concluding remark, implications

We developed a brittle creep and brittle failure model recognizing that flaws in rocks exist over a broad range of length-scales. Our assumption behind the model is motivated by the fact that self-similarity is one of the characteristics of brittle systems; grain size distributions in fault rocks (e.g. Keulen et al. 2008), roughness of frictional interfaces (e.g. Candela et al. 2012), acoustic emissions recorded during experiments (e.g. Goebel et al. 2017), as well as moment-magnitude scaling of crustal earthquakes (Gutenberg and Richter 1944) are all suggesting that cracking is a process that is self-similar over many orders of magnitude in length scale. The interactions of the dominant microcracks with smaller flaws in their vicinity, leads to their coalescence, formation of micro shear bands and eventually to shear failure when the growing dominant shear band reaches the sample boundaries, as typically observed in rocks deformed under confining pressure. In our model, both the inclined dominant microcracks as well as their associated wing cracks are allowed to grow in contrast to traditional models of brittle creep where only wing crack growth is assumed (e.g. Ashby and Sammis 1990, Brantut et al. 2012). Comparison of our model to experimental data suggests that the complex and non-tractable interactions of the rock microcracks and flaws can be adequately expressed by the simple power law functions,  $f(L) = (L/\Lambda)^q$ , where  $L$  is the normalized wing crack length and  $\Lambda$  represents the normalized distance over which a wing crack must propagate to interact with other flaws. The model reproduces all three characteristic stages of creep and returns experimentally determinable quantities, namely the ratio of time to failure,  $t_F$ , to the time of minimum wing crack propagation velocity (i.e. minimum strain rate, or center of the secondary creep segment),  $t_2$ , and a power-law exponent,  $m$ , that characterizes the mean deceleration rate of primary creep. The model successfully fits data from a broad range of rocks and - with appropriate normalization and accounting for elastic deformation - can be also used to model brittle failure. Furthermore, our model predicts that brittle creep can occur over a very broad range of flaw densities and/or stress levels depending on the exact functional form. Tertiary, accelerating creep has typically been observed only at a high percentage (>50%) of the ultimate failure strength (e.g. Brantut et al. 2012), however recent experiments document primary and secondary brittle creep operating at stress levels as low as ~10% of the failure strength (Xing et al. 2022) providing evidence that brittle creep indeed occurs over a broad range of stress levels – resolving whether creep at such low fractions of the failure strength will eventually enter the tertiary creep stage is however impossible in the laboratory. As shown in figure 8, the time to failure predicted by the model varies by over 20 orders of magnitude for the variations of  $\Lambda$  explored in this work.

#### 5. Conclusions

We reformulated the wing crack model of brittle creep and brittle failure to allow for the formation, growth and coalescence of micro shear bands over a broad range of length scales and found that:

- The model using a wide class of function  $A(L)$  properly returns classical trimodal creep curves for constant stress boundary conditions and characteristic stress-strain curves under constant strain rate boundary conditions



- The model returns experimentally determinable quantities independent of the chosen normalizations. Key outputs are the ratio of time to failure,  $t_F$ , to the time of minimum strain rate,  $t_2$ , and a power-law exponent,  $m$ , that characterizes the mean deceleration rate of primary creep.
- The function  $A(L) = 1 + f(L)$ , where  $f(L)$  is a simple power law,  $f(L) = (L/\Lambda)^q$ , produced values of the constants  $\Lambda$  and  $q$  consistent with those estimated from the experimental data. The parameter  $\Lambda$  represents a normalized distance over which a flaw must propagate to interact with other flaws and can be related to flaw density and stress level.
- Polynomial functions which combine the effect of multiple terms with different degrees, yielded results inconsistent with the experimental data, suggesting that brittle creep of rocks can be appropriately described using the power law function,  $f(L) = (L/\Lambda)^q$ .

## Appendix A

The limit  $\Lambda_c$  is the upper limit of  $\Lambda$  such that the curves of  $\sqrt{1 + (L/\Lambda_c)^q}$  and  $\sqrt{L}$  versus  $L$  are tangent. As discussed in section 2.3, the two curves do not intersect when  $\Lambda$  is smaller than  $\Lambda_c$  and they intersect on two separate points for  $\Lambda$  strictly larger than  $\Lambda_c$ . We now note that the curves produced by elevating the two functions above to the power 2 are also tangent to each other for  $\Lambda = \Lambda_c$ . They therefore have a single common point, where the derivatives of the functions with respect to  $L$  must be equal. We can therefore write the two obvious equalities  $1 + (L/\Lambda_c)^q = L$  and  $q (L^{q-1}/\Lambda_c^q) = 1$ . Eliminating  $L$  between these two equations yields  $\Lambda_c = (q^{1/(1-q)} - q^{q/(1-q)})^{(1-q)/q}$ .

## Appendix B

We wish to calculate the coordinates  $\tau^*_{\text{peak}}$  and  $l^*_{\text{peak}}$  of the maximum of the curve of  $\tau^*$  versus  $l^*$  predicted by equation 15. For this, we only need to calculate the derivative with respect to  $l^*$  of the right-hand side of equation 15:

$$\tau'(l^*) = \frac{1 + \left(\frac{l^*}{\lambda^*}\right)^q - q \left(\frac{l^*}{\lambda^*}\right)^q}{2\sqrt{l^*} \left(1 + \left(\frac{l^*}{\lambda^*}\right)^q\right)^{3/2}}$$

Solving  $\tau'(l^*) = 0$  for  $l^*$  yields the solution  $l^*_{\text{peak}} = \lambda^*/(q-1)^{1/q}$  and plugging this value in equation 15

produces  $\tau^*_{\text{peak}} = \sqrt{\frac{\lambda^*}{q} (q-1)^{\frac{q-1}{q}}}$ , which can be rewritten  $\tau^*_{\text{peak}} = \sqrt{l^*_{\text{peak}} (q-1)/q}$ .

## Data Availability Statement

Our model is analytical. Computer programming is therefore unnecessary in principle. However certain parameters such as the power law exponent  $m$  are easier to determine numerically. To help interested readers, the Mathematica script used to construct and interpret Figure 8 is available at Zenodo. Except for the Iceland and Etna 2 basalts, we used published experimental data that can be obtained from the articles cited. The Iceland and Etna 2 basalts data were produced in our laboratory and are available at Zenodo at 10.5281/zenodo.6463941.

## References

- Ashby, M.F., and S.D. Hallam (1986), The failure of brittle solids containing small cracks under compressive stress states, *Acta Metall.*, 34, 497-510.
- Ashby, M.F., and C.G. Sammis (1990), The damage mechanics of brittle solids in compression, *PAGEOPH*, 133(3), 489-521.

- Baud, P., T. Reuschlé and P. Charlez (1996), An improved wing crack model for the deformation and failure of rock in compression, *Int. J. Rock Mech. Min. Sci. Geomech. Abstr.*, 33, 539-542.
- Bernabé, Y., D.T. Fryer and R.M. Shively (1994), Experimental observations of the elastic and inelastic behaviour of porous sandstones, *Geophys. J. Int.*, 117, 403-418.
- Brantut, N., P. Baud, M.J. Heap, and P.G. Meredith (2012), Micromechanics of brittle creep in rocks, *J. Geophys. Res. - Solid Earth*, 117, B08412, doi: 10.1029/2012JB009299.
- Brantut, N., M.J. Heap, P.G. Meredith and P. Baud (2013), Time-dependent cracking and brittle creep in crustal rocks: a review, *J. Struct. Geol.*, 52, 17-43.
- Brantut, N., M.J. Heap, P. Baud and P.G. Meredith (2014a), Mechanisms of time-dependent deformation in porous limestone, *J. Geophys. Res. - Solid Earth*, 119, 5444-5463, doi:10.1002/2014JB011186.
- Brantut, N., M.J. Heap, P. Baud and P.G. Meredith (2014b), Rate- and strain-dependent brittle deformation of rocks, *J. Geophys. Res. - Solid Earth*, 119, 1818-1836, doi:10.1002/2013JB010448.
- Charles, R.J. (1958), Static fatigue of glass, II, *J. Appl. Phys.*, 29(11), 1554-1560.
- Desrues, J. (1990), Shear band initiation in granular materials: experimentation and theory, in *Geomaterials: Constitutive Equations and Modelling* (ed. F. Darve), Elsevier Applied Science, 283-310.
- Desrues, J., and E. Andó (2015), Strain localization in granular media, *C.R. Physique*, 16, 26-36.
- Fortin, J., S. Stanchits, G. Dresen and Y. Guéguen (2009), Acoustic emissions monitoring during inelastic deformation of porous sandstone: comparison of three modes of deformation, *PAGEOPH*, doi: 10.1007/s00024-009-0479-0.
- Fortin, J., S. Stanchits, S. Vinciguerra and Y. Guéguen (2010), Influence of thermal and mechanical cracks on permeability and elastic wave velocities in a basalt from Mt. Etna volcano subjected to elevated pressure, *Tectonophysics*, 503(1-2), 60-74.
- Fujii, Y., T. Kiyama, Y. Ishijima and J. Kodama (1999), Circumferential strain behavior during creep tests of brittle rocks, *Int. J. Rock Mech. Min. Sci.*, 36, 323-337.
- Goebel, T. H. W., Kwiatek, G., Becker, T. W., Brodsky, E. E., & Dresen, G. (2017). What allows seismic events to grow big?: Insights from b-value and fault roughness analysis in laboratory stick-slip experiments. *Geology*, 45(9), 815–818. <https://doi.org/10.1130/G39147.1>
- Gutenberg, B., & Richter, C. F. (1944). Frequency of earthquakes in California. *Bulletin of the Seismological society of America*, 34(4), 185-188.
- Heap, M.J., and D.R. Faulkner (2008), Quantifying the evolution of static elastic properties as crystalline rock approaches failure, *Int. J. Rock Mech. Min. Sci.*, 45, 564-573.
- Heap, M.J. (2009), *Creep: Time-dependent Brittle Deformation in Rock*, PhD Thesis, University College London, pp. 399.
- Heap, M.J., P. Baud, P.G. Meredith, A.F. Bell and I.G. Main (2009), Time-dependent brittle creep in Darley Date sandstone, *J. Geophys. Res. Solid-Earth*, 114, B07203, doi: 10.1029/2008JB006212.
- Heap, M.J., P. Baud, P.G. Meredith, S. Vinciguerra, A.F. Bell and I.G. Main (2011), Brittle creep in basalt and its application to time-dependent volcano deformation, *Earth Planet. Sci. Lett.*, 307, 71-82.
- Horii, H., and S. Nemat-Nasser (1985), Compression-induced microcrack growth in brittle solids: axial splitting and shear failure, *J. Geophys. Res.*, 90(B4), 3105-3125.
- Kachanov, M.L. (1982), a microcrack model of rock inelasticity. Part II: propagation of microcracks, *Mech. Materials*, 1, 29-41.
- Keulen, N., Heilbronner, R., Stünitz, H., Boullier, A.-M., & Ito, H. (2007). Grain size distributions of fault rocks: A comparison between experimentally and naturally deformed granitoids. *Journal of Structural Geology*, 29(8), 1282–1300.
- Lajtai, E.Z. (1974), Brittle fracture in compression, *Int. J. Fract.*, 10, 525-536.
- Lin, Q.B., P. Cao, G.P. Wen, J.J. Meng, R.H. Cao and Z.Y. Zhao (2021), Crack coalescence in rock-like specimens with two dissimilar layers and pre-existing double parallel joints under uniaxial compression, *Int. J. Rock Mech. Min. Sci.*, 139, 104621, doi: 10.1016/j.ijrmms.2021.104621.

- Lockner, D.A., J.D. Byerlee, V. Kuksenko, A. Ponomarev and A Sidorin (1992), Observations of quasistatic fault growth from acoustic emissions, in *Fault Mechanics and Transport Properties of Rocks* (eds. B. Evans and T-f. Wong), Academic Press, 3-31.
- Lockner, D.A. (1993), The role of acoustic emissions in the study of rock fracture, *Int. J. Rock Mech. Min. Sci. & Geomech. Abstr.*, 30(7), 883-899.
- Lockner, D.A. (1998), A generalized law for brittle deformation of Westerly granite, *J. Geophys. Res.*, 103(B3), 5107-5123.
- Main, I.G. (2000), A damage mechanics model for power-law creep and earthquake aftershock and foreshock sequences, *Geophysical Journal International*, 142(1), 151–161, doi: 10.1046/j.1365-246x.2000.00136.x.
- Mallet, C., J. Fortin, Y. Guéguen and F. Bouyer (2014), Evolution of the crack network in glass samples submitted to brittle creep conditions, *Int. J. Fract.*, 190, 111-124, doi: 10.1007/s10704-014-9978-9.
- Mallet, C., J. Fortin, Y. Guéguen and F. Bouyer (2015), Brittle creep and subcritical crack propagation in glass submitted to triaxial conditions, *J. Geophys. Res. Solid Earth*, 120, 879-893, doi: 10.1002/2014JB011231.
- Mansbach, Elias. 2022. "Effect of Carbon Sequestration and Reservoir Conditions on Brittle Creep in Etna Basalt." Thesis Commons. Doi: 10.31237/osf.io/64gxc
- Rawling, G.C., P. Baud and T-f. Wong (2002), Dilatancy, brittle strength, and anisotropy of foliated rocks: experimental deformation and micromechanical modeling, *J. Geophys. Res. Solid-Earth*, 107, B10, 2234, doi: 10.1029/2001JB000472.
- Stanchits, S., S. Vinciguerra and G. Dresen (2006), Ultrasonic velocities, acoustic emission characteristics and crack damage of basalt and granite, *PAGEOPH*, 163, 974-993, doi: 10.1007/s00024-006-0059-5.
- Wiederhorn, S.M., and L.H. Bolz (1970), Stress corrosion and static fatigue of glass, *J. Am. Ceram. Soc.*, 53(10), 543-548.
- Wong, N.Y. (2008), *Crack Coalescence in Molded Gypsum and Carrara Marble*, PhD Thesis, MIT, pp. 876.
- Wong, N.Y. and H.H. Einstein (2009a), Crack coalescence in molded gypsum and Carrara marble: part 1-macroscopic observations and interpretations, *Rock Mech. Rock Eng.*, 42(3), 475-511.
- Wong, N.Y. and H.H. Einstein (2009b), Crack coalescence in molded gypsum and Carrara marble: part 2-microscopic observations and interpretation, *Rock Mech. Rock Eng.*, 42(3), 513-545.
- Xing, T., H.O. Ghaffari, U. Mok and M. Pec (2022), Creep of CarbFix basalt: influence of rock-fluid interaction, *Solid Earth*, 13, 137–160, <https://doi.org/10.5194/se-13-137-2022>
- Zoback, M. L., & Zoback, M. (2007). Lithosphere Stress and Deformation. In G. Schubert (Ed.), *Treatise on Geophysics (Second Edition)* (pp. 255–271). Elsevier, doi: 10.1016/B978-0-444-53802-4.00115-9.